JACS
JOURNAL OF THE AMERICAN CHEMICAL SOCIETY
pubs.acs.org/JACS
Article

Electrostatic and Electronic Effects on Doped Nickel Oxide Nanofilms for Water Oxidation

Ina Østrøm, Marco Favaro, Moein Seyfouri, Patrick Burr, and Bram Hoex*

Cite This: https://doi.org/10.1021/jacs.4c14493
Read Online
ACCESS | Metrics & More | Article Recommendations | Supporting Information

ABSTRACT: An ideal water-splitting electrocatalyst is inexpensive, abundant, highly active, stable, selective, and durable. The anodic oxygen evolution reaction (OER) is the main bottleneck for H_2 production with a complex and not fully resolved mechanism, slow kinetics, and high overpotential. Nickel oxide-based catalysts (NiO_x) are highly active and cheaper than precious metal catalysts. However, rigorous catalyst tests and DFT calculations are still needed to rationally optimize NiO_x catalysts. In this work, we combine plasma-enhanced atomic layer deposition (PE-ALD) and density functional theory (DFT) to address the role of dopants in promoting NiO_x OER activity. Ultrathin films of NiO_x doped with Zn^{2+}, Al^{3+}, and Sn^{4+} presented improved intrinsic activity, stability, and durability for the OER. The results show a low to high catalytic performance of $ZnNiO_x$ < NiO_x < $AlNiO_x$ < $SnNiO_x$, which we attribute to an increase in the concentration of valence band (VB) holes combined with conduction band (CB) electron conductivity, characterized by electrochemical impedance spectroscopy (EIS). The influence of doping on the electronic structure and catalytic activity was investigated using advanced characterization techniques and density functional theory (DFT) calculations (PEB0/pob-TZVP). DFT complements the experimental results, showing that the dopant charge states and orbital hybridization enhance the OER by improving the charge carrier concentration and mobility, thus allowing optimal binding energies and charge dynamics and delocalization. Our findings demonstrate the potential of PE-ALD-doped nanofilms NiO_x and DFT to rationally design and develop catalysts for sustainable energy applications.

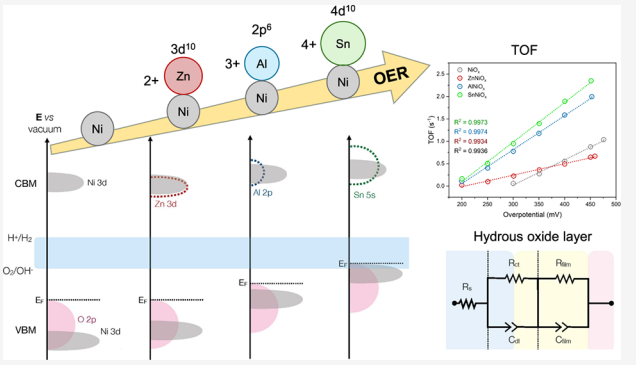

INTRODUCTION

The oxygen evolution reaction (OER) is critical for the technological revolution in the energy conversion landscape.[1] For example, in hard-to-abate industry sectors, the OER can have an impact on sustainability through processes such as energy production and storage (e.g., green hydrogen and batteries), carbon capture (e.g., artificial photosynthesis through CO_2 reduction), and production of fertilizers (e.g., artificial nitrogen fixation for green ammonia).[2−7] Hence, improving the efficiency of the OER can lead to industrial development and commercialization of technologies capable of meeting global targets for net-zero carbon emissions by 2050.[8,9]

The OER has a complex multistep mechanism − hindered both kinetically and thermodynamically − that is assumed to follow a four-electron transfer adsorbate evolution mechanism (AEM), with the adsorbed (*) oxygen intermediate species *OH, *O, and *OOH, or the two-electron transfer lattice oxygen mechanism (OEM).[10−13] This kinetic inefficiency is one of the key contributors to the high overpotential (200 mV in acid and 300 mV in base at 10 mA/cm^2) for the state-of-the-art IrO_2 and RuO_2 OER catalysts, resulting in high cost and low energetic efficiency for industrial and commercial applications.[14−16] To address this, low-cost, earth-abundant transition metal oxide (TMO) catalysts, such as NiO_x, can be used in alkaline media and are known to be highly active and stable. Thus, optimizing and promoting NiO_x activity, stability, durability, and selectivity for the OER is critical.[14,17,18] Still, the hasty and unruly growth in the field of electrocatalysis remains rich in inconsistency, discussions, and catalysts with complex structures that hinder scientific and engineering progress to accelerate industrial and global development.[19−26]

The intrinsic properties of TMOs and their OER activity depend on the structure of the solid−electrolyte interface (SEI). The advances made in characterizing the SEI and connecting TMO properties to the OER activity involve: (a) *in situ operando* spectroscopic techniques to probe crystalline phase transformation under operational conditions (e.g., hydroxide/oxyhydroxide formation); (b) rationalization of

Received: October 31, 2024
Revised: January 9, 2025
Accepted: January 10, 2025

the role of different metal dopants (e.g., Cr^{n+}, Mn^{n+}, Fe^{n+}, Co^{n+}, Ce^{n+}, La^{3+}, Al^{3+}, and Li^{+}) in promoting OER activity; (c) the effects of an applied magnetic field on the spin-polarized interaction between the O_2 *p*-orbital triplet state with the unpaired metal *d* electrons; (d) atomistic-level density functional theory (DFT) modeling of OER thermodynamics through the computational hydrogen electrode (CHE) model and microkinetics analysis of activation energies and transition state stabilization, assuming that the OER mechanism occurs via the adsorbate evolution mechanism (AEM) or the lattice oxygen oxidation mechanism (LOM); (e) scaling-relationship descriptors, e.g., $\Delta\Delta G_{*O-*OH}$, number of excess electrons, *d*-electrons, covalency (i.e., hybridization of orbitals in M−O bonds), e_g occupancy, electrostatic (Madelung potentials), TM electronegativity, and oxophilicity; and (f) beyond DFT modeling of electrochemical proton-coupled electron transfer and simulation of the electric double-layer (EDL) processes including implicit solvation, charged surfaces with constant potentials, and real-space codes enabling grid-based mapping of the free energies as a function of potential.[12,13,27−40]

These electronic properties depend on multiple electronic effects that result from the nature of the M^{n+}−O bonding, which affects the adsorption of the OER oxygen intermediate species and the stabilization of the transition states. For example, the crystal structure (e.g., rocksalt, spinel, and perovskite oxides) rules the metal oxidation states; synergistic effects of cation and oxygen defect formation affect the mechanistic pathways favored by the OEM in contrast to the AEM (and vice versa); and changes in the semiconductivity lead to reduced charge-transfer resistances.[10,12,14,29,41−44] In the case of the strongly correlated 3*d* TMOs, other factors arise due to the low energy barriers of coupling interactions and competing mechanisms between spin, orbital, lattice, and charge.[26] Some examples of electronic properties that result from such degrees of freedom are ferroelectricity, magneto-electricity, spin−orbit coupling, and orbitronics, which can play a role in the OER. In heavier 5*d* TMOs, for example, IrO_2 and RuO_2, relativistic shielding effects of the nuclei make the 5*d* valence electrons more loosely bound. Hence, the choice of the M^{n+} added to NiO_x is critical to rationalizing the intrinsic properties of catalysts to the OER and understanding how and why catalytic activity is promoted.

This work employs plasma-enhanced atomic layer deposition (PE-ALD) to investigate the role of doping effects of Zn^{2+}, Al^{3+}, and Sn^{4+} on NiO_x in enhancing the OER. PE-ALD offers advantages related to process control, temperature-dependent epitaxially growth of crystalline structures, and thickness control to produce a conformal ultrathin film of supportless catalysts.[45] These metal cations were selected − in contrast to most studied 3d TMs (e.g., Mn^{n+}, Fe^{n+}, and Co^{n+}) − because they are OER inactive, closed-shell, and each has only one highly favorable oxidation state (Zn^{2+} [$4s^0$, $3d^{10}$], Al^{3+} [$3s^0$, $3p^0$], and Sn^{4+} [$4d^{10}$, $5s^05p^0$]), with different charge states. We combine experiments with hybrid DFT and all-electron basis sets to demonstrate how and why Zn^{2+}, Al^{3+}, and Sn^{4+} promote or hinder the NiO_x OER activity. We compare our modeled materials to the doping effect of Fe^{n+} ($n = 2+, 3+, 4+$) on NiO_x, known as the best NiO_x promoter for the OER due to a combination of electronic effects that is not yet fully understood.[46]

EXPERIMENTS AND METHODS

Plasma-Enhanced Atomic Layer Deposition. Nickel oxide-based catalysts were prepared by plasma-enhanced atomic layer deposition (PE-ALD) in a Veeco-Ultratech/Cambridge NanoTech Fiji G2 system, equipped with an in situ quartz crystal microbalance (QCM) (Inficon, STM-2) and a spectroscopic ellipsometer (SE) (J.A. Woollam, model M-2000) (Figure S1). The catalyst films were deposited on fluorine-doped tin oxide (FTO)-coated glass (Hartford Glass, TEC 8, MSE Supplies) for the electrochemical tests, and on Czochralski (Cz) single-side polished wafers, 500 μm thick, and low-resistivity (B-doped p-type, 0.001−0.005 $\Omega\cdot cm^{-1}$, University Wafer) for in situ SE and other characterization techniques. Different dimensions of the FTO substrate were used for electrochemical tests in the flow cell (25 × 25 mm) and standard sealed cell (10 × 20 mm). The film deposition area (0.5 cm^2) of the 10 mm × 20 mm substrates was controlled using Kapton tape. Details about the PE-ALD recipes, SE modeling, and the cleaning process of the FTO and Si substrates can be found in the Supporting Information.

Electrochemical Measurements. The electrochemical activity was studied using two different systems: (i) 1 M reagent-grade KOH (ChemCruz, 86.7%) with Milli-Q water (ρ = 18.2 MΩ·cm) as the solvent, in a custom-made polytetrafluoroethylene (PTFE) flow cell with a 1.33 cm^2 nominal area of exposure of the thin film as the working electrode (WE) (FTO 25 × 25 mm with Cu tape for electrical connection) and equipped with a Pt wire as the counter electrode (CE), and a miniaturized leakless Ag/AgCl as the reference electrode (RE). This setup utilized a peristaltic pump for the electrolyte flow (see Figure S4 for setup images) and a Bio-Logic SP-300 potentiostat; (ii) 30 mL of 1 M KOH (Sigma-Aldrich, 99.99%, Milli-Q water) purged for 20 min in N_2 in a standard sealed cell (100 mL) that exposed 0.5 cm^2 of the catalyst film in FTO (10 × 20 mm) immersed in the alkaline solution, with a Pt wire CE (RedoxMe) and Ag/AgCl (3.5 M KCl, RedoxMe) RE. The catalytic activity of the films was tested in this setup with a Metrohm Multi Autolab/M204, and the Ag/AgCl RE was recalibrated against another Ag/AgCl after each catalyst test. The reversible hydrogen electrode potential (U_{RHE}) was related to the Ag/AgCl (25 °C, 3.5 M KCl) electrode and the electrolyte pH according to ($E^{o}_{Ag/AgCl}$ = 0.1976 V):

$$E_{RHE} = E_{Ag/AgCl} + E^{o}_{Ag/AgCl} + 0.0591 \times pH \quad (1)$$

The different catalyst films OER activities were tested several times, and the results shown here are the optimized results. The open circuit potential (OCP) was measured for 60 s before each experiment to guarantee valid electrical connections before the OER testing of the samples. The films were exposed to the electrolyte for 45 min at the OCP to allow catalyst wetting. After wetting, the preconditioning (or aging) of the films was performed through cyclic voltammetry (CV) (1 to 1.7 V vs U_{RHE} at a slow scan rate of 20 mV/s) to allow reconstruction of the as-deposited oxide films into the hydroxide/oxyhydroxide species. Conditioning consisted of scanning the potential for up to 600 cycles (>20 h) until the Ni^{2+}/Ni^{3+} redox peak wave stabilized in size and position. This procedure tests the stability of the catalyst and allows its reconstruction and adaptation to anodic potentials and alkaline media to form the most active catalyst form, as previously observed.[27,29,47] The films were allowed to rest at the OCP for

https://doi.org/10.1021/jacs.4c14493
J. Am. Chem. Soc. XXXX, XXX, XXX−XXX

at least 1 h to recover and equilibrate with the electrolyte. The catalytic activity for the Tafel analysis was measured with linear sweep voltammetry (LSV) at a scanning rate of 1 mV/s and a rate of 70 rpm (flow cell) and at 0.1 mV/s in the standard cell under static conditions. Chronoamperometry (CA) was employed as a static electrocatalytic activity test at 445 mV overpotential for 1 h. The long-term stability of $SnNiO_x$ was tested using chronopotentiometry (CP) at 10 mA/cm^2.

The uncompensated series resistance (*iR* drop) of the electrolyte was obtained by electrochemical impedance spectroscopy (EIS) under static conditions and by OCP, using a Pt foil (1.13 Ω) as the WE in the flow cell and plain FTO (10 Ω) in the standard cell. All electrochemical studies were performed at room temperature (25 °C). EIS was used to study the behavior of the capacitance and resistances as a function of the overpotential (300−500 mV) for kinetics, and in a non-Faradaic region (1.12 V) for the electrochemically active surface area (ECSA). For these measurements, the frequency range was from 10 kHz to 0.1 Hz, with an AC amplitude of 10 mV. The validity of the EIS data obtained was checked via Kramers−Kronig (KK) relations and modeled using one or two Randle's circuits with constant phase elements (CPE). The ECSA was also obtained by sweeping the potential from 1.12 to 1.22 V with a 10 s pause at the vertex potentials and a gradient of the scan rates (2.5, 5, 10, 15, 25, and 50 mV/s). We redirect the reader to the Supporting Information for a detailed descriptive analysis of the catalyst conditioning, electrocatalytic tests, EIS fitting, and plots.

Film Structure, Composition, and Morphology. Film thicknesses and optical properties were investigated on Si wafer and FTO substrates with a J.A. Woollam M-2000 that allowed angle variations between 65° and 70°, in a spectral range from 1.0 to 5.0 eV. The ratio of the amplitudes of the reflected polarized light components (Ψ) and the phase shift introduced between them (Δ) was analyzed with the CompleteEASE software (v6.42). The model consists of a silicon substrate with a native oxide layer (2 nm of a thermal SiO_2 layer) capped by a metal oxide on top. Two Tauc−Lorentz (TL) oscillators with AFM roughness were used to fit the dispersion of the optical dielectric functions and obtain film thickness, optical bandgap, and dielectric constant.[48,49] Time-of-flight secondary ion mass spectrometry (ToF-SIMS) (ION-TOF GmbH, Münster, Germany) confirmed the film composition and revealed a depth profile analysis of elements in the films. For the metallic elements, a positive polarity Bi^+ (30 keV) sputter O_2^+ beam (500 eV) was used, and for the nonmetallic elements, a negative polarity Bi^+ (30 keV) sputter Cs^+ beam (1000 eV) was used. Inductively coupled plasma mass spectrometry (ICP-MS), in open acid digestion (3 HCl + 1 HNO_3), was performed to quantify metallic elements in the films before and after the OER.

The crystal structures and texture coefficients were obtained with grazing incidence angle X-ray diffraction (GIXRD) collected at 0.5°, using a PANalytical Xpert Materials Research Diffractometer (MRD) system with CuKα radiation (1.5406 Å) at a scan rate of 0.01°/s. The film roughness was studied with atomic force microscopy (AFM), using an Asylum Cypher system from Oxford Instruments. The imaging was performed in tapping mode using a conductive Cr/Pt-coated tip (Multi75E-G BudgetSensors) with a resonant frequency of 75 kHz and a force constant of 3 N/m. The oxidation state and chemical bonding of M−O in the films were studied with X-ray photoelectron spectroscopy (XPS) measurements (ESCALAB 250Xi, Thermo Scientific) using a monochromatic Al Kα X-ray source with an energy of 1486.68 eV and a binding energy (BE) reference (C 1s) for adventitious carbon. The electronic structures were reconstructed from ultraviolet photoelectron spectroscopy (UPS), using a He(I) discharge source ($h\nu$= 21.2 eV) with a passing energy of 2 eV, and 15 s of Ar plasma was used to clean the film surface. Field-emission scanning electron microscopy (FE-SEM) (FEI NanoSEM 450) was used for ultrahigh imaging resolution of film morphologies on Si and FTO substrates (before and after the OER), with Schottky field-emission at 15 kV and 0.2 nA current. Aberration-corrected scanning transmission electron microscopy (STEM) (200 kV, JEOL F200 TEM) was used to image the cross-section of the TMO films, visualize crystalline morphology and confirm chemical composition with electron dispersive X-ray spectroscopy (XEDS) (JEOL 100 mm^2 Silicon drift) in Si wafer samples.

Computational Details. Density functional theory (DFT) calculations were performed with the CRYSTAL17 code.[50,51] The PBE0 hybrid density functional (25% of Fock exchange) was used in combination with high-quality all-electron Gaussian triple ζ valence with polarization (pob-TZVP) basis sets, which are suitable for solid-state calculations and corrected for basis set superposition error (BSSE).[52,53] We have previously shown that this functional and basis set choice is adequate to model NiO_x.[26] A spin-polarized unrestricted Kohn−Sham approach was used to describe the antiferromagnetic AFM-II spin ordering of NiO_x. Grimme's empirical D3 long-range dispersion correction was used with Becke-Johnson damping (BJ).[54,55] The NiO_x bulk supercell (64 atoms) and slabs containing neutral and charged point defects were fully relaxed and optimized using an 8 × 8 × 8 *k*-points mesh. The TMO (111) surfaces were modeled with five atomic monolayers, with two lower layers fixed to mimic the bulk, relaxing the top three layers under vacuum (500 Å) and an 8 × 8 × 1 *k*-points mesh. The NiO_x (111) Tasker type III polarized surface was balanced by removing excess oxygen atoms, thus creating neutral oxygen vacancies. Optimizations were performed with a total energy convergence criterion of 10^{-8} E_h, with the default integration grid.

The Coulomb and exchange integral truncation tolerance factors, the penetration threshold of the Coulomb integrals, and the overlap threshold of the HF exchange integrals were set to 10^{-8}, and 10^{-16} for pseudooverlap in the HF exchange series. All structures were confirmed to have no negative eigenvalues in the estimated Hessian. An extra-large pruned integration grid was used for higher accuracy in the Hirshfeld charge population analysis. Coupled perturbed Kohn−Sham (CPKS) was applied to the slabs with 8 × 8 × 1 *k*-points.[56,57] Denser *k*-point meshes were used for band structures (16 × 16 × 16) and density of states (DOS) (12 × 12 × 12). High-symmetry points of the reciprocal space were chosen to plot the *k*-vector paths of the first Brillouin zone, which correspond to real space for interpretation in the face-centered cubic crystal of NiO_x.[58] We evaluated two monoelectronic properties of the TMO slabs at the atomic positions superimposed by an isosurface of the electron density and spin density (0.0005 cutoff, electron/Å^3, visualized in VESTA), to illustrate charge distribution colored by electrostatic potentials and the electronic and spin densities.[59] Theoretical details and definitions of derived properties, such as the work function

https://doi.org/10.1021/jacs.4c14493
J. Am. Chem. Soc. XXXX, XXX, XXX−XXX

Table 1. Key OER Activity Indicators[a]

Catalyst	η_{10} (mV)	TOF (s^{-1})	TON (1 h)	C_{film}(mF/cm^2)	R_{film}(Ω/cm^2)	T_f (mV/dec)
NiO_x	406	0.57 (400 mV)	2.40	1.19 (340 mV)	121.90 (340 mV)	41
$ZnNiO_x$	296	0.49 (400 mV)	1.80	2.03 (340 mV)	109.68 (340 mV)	44
$AlNiO_x$	267	1.58 (400 mV)	5.80	2.00 (340 mV)	172.12 (340 mV)	42
$SnNiO_x$	262	1.86 (400 mV)	8.90	2.14 (340 mV)	107.40 (340 mV)	44

[a] η_{10} = overpotential at 10 mA/cm^2, TOF = turnover frequency, TON = turnover number, C_{film} = film capacitance, R_{film} = film resistance, and T_f = Tafel slope.

(ϕ), electron (m_e^*), and hole (m_h^*) effective mass, can be found in the Supporting Information.

RESULTS AND DISCUSSION

Electrochemical Performance. The main activity indicators are summarized in Table 1 and illustrated in Figure 1. A benchmark comparing the published results can be found in Table S2, including relevant information about the synthesis, substrate, and electrolyte used. The analysis of CV activation of the catalysts (Figures S5−S7) and the expressions used to derive the catalytic activity can be found in the Supporting Information. The apparent catalytic activity is given by the amount of overpotential necessary to produce 10 mA/cm^2 and was found in the ascending order of $SnNiO_x$ (262 mV), $AlNiO_x$ (267 mV), $ZnNiO_x$ (296 mV), and NiO_x (406 mV) [Figure 1a]. From our TOF results, the intrinsic catalytic activity decreases in the order of $SnNiO_x$ > $AlNiO_x$ > NiO_x > $ZnNiO_x$, with NiO_x overcoming $ZnNiO_x$ at above 400 mV overpotential [Figure 1c]. The activity of $SnNiO_x$ in FTO (η_{10} = 262 mV, TOF = 1.86 s^{-1} at 400 mV in 1 M KOH) is comparable to their best catalyst $Fe_{0.1}$-NiO_x (η_{10} = 234 mV, TOF = 1 s^{-1} at 350 mV in 1 M KOH). Bent et al. studied thin films of NiO_x to $AlNiO_x$ produced with thermal O_3 ALD and compared the film activities of different Fe electrolyte concentrations.[29] In all electrolytes tested, $AlNiO_x$ had better OER activity than NiO_x. Their $AlNiO_x$ film was produced with thermally heated O3 ALD and saturated with Fe in the electrolyte (0.1 M KOH). Our $AlNiO_x$ film presented higher activity compared to their results (η_{10} = 267 mV, TOF = 1.86 s^{-1} at 400 mV in 1 M KOH), and a dedicated study comparing PE-ALD to thermal ALD, under identical process conditions, is necessary to confirm if PE-ALD catalysts are more active.[27] Lloret-Fillol et al. studied M^{n+}-doped self-supported NiO_x films in Ni foam (NF) (M = Fe^{3+}, Co^{2+}, Mn^{2+}, Zn^{2+}) (Table S2) and found that doping NiO_x with Zn had the worst OER activity, and Fe had the best OER activity of all studied metals.[30] Their reported OER activity used an NF substrate, making it challenging to identify the real catalytic response since NF is OER active.[60]

The Tafel slope (T_f) in Figure 1b informs us about the OER mechanism, and the exchange current density (i_0) is a measure of the intrinsic current when the catalyst is at equilibrium with the environment. The latter is related to charge-transfer resistance (R_{ct}) such that low i_0 is associated with higher R_{ct}, consequently, slower electron transfer kinetics.[61] From the T_f plots in Figure 1, i_0 was found to decrease in magnitude in the descending order of NiO_x > $SnNiO_x$ > $AlNiO_x$ > $ZnNiO_x$. The T_f of 40 mV/dec, measured at 1 mV/s to ensure the steady-state current condition, suggests that the OER mechanisms are identical. The same T_f slope was obtained in plots where the ECSA normalized the current in the standard cell under static conditions (Figure S8). Xiao et al. combined grand-canonical methods and microkinetic modeling to study the potential dependence of the OER mechanism for NiO_x-based hydroxides.[62] According to their results and the Tafel slope microkinetic analysis from Takanabe, we associate T_f = 40 mV/dec to the AEM with optimal binding energies for the OER intermediate and a first-order mechanism (d) that can be either EE* or ECE* [E = electrochemical, C = chemical, and * = rate-determining step (RDS)].[63−65] In both cases, the RDS is electrochemical and refers to the second proton-coupled electron transfer, assuming a single-site mechanism in alkaline media, involving 2 or 4-electron transfer (M* = metal site). According to Takanabe et al., the RDS depends on the formation of O−O bonds with the predominant surface species being *OH and *O.[63,66] Furthermore, Nørskov et al.'s work supports that idea using thermodynamic and kinetic models that show that the optimal OER activity can be predicted by the volcano relations of the overpotential as a function of $\Delta G_{*O} - \Delta G_{*OH}$.[35]

The EIS was obtained at different potentials in the OER Faradaic region, using an Armstrong−Henderson circuit to describe the two semicircles of the Nyquist plots (Figure 1f, and fit error analysis in Tables S5 and S6).[67] The elements selected to model the EIS, as shown in Figure 1f, were the double-layer capacitance (C_{dl}), charge-transfer kinetics (R_{ct}), film capacitance from dynamics of adlayers (C_{film}), and the film adsorption resistance (R_{film}).[67] Figure 1d,e shows how C_{film} and R_{film} change from pristine (after 20 CV cycles) to aged (after 600 CV cycles) as a function of the applied potential (see the arrow). The magnitude of C_{film} (mF) reflects the formation of the hydrous porous layer of TMO, where other ionic species of the electrolyte permeate.[68] The small semicircle at the higher frequency of the Bode plots under the active potentials of the OER is attributed to the EDL. This semicircle is absent in non-Faradaic potentials and on plain FTO at all potentials (Figure S12).

The EDL does not change with the applied potential but changes with the formation of the activated NiOOH hydrous catalyst (Figures S11−S16). Maillard et al. and Strasser et al. revisited the determination of the ECSA of TMO measured by EIS for the OER in the Faradaic region and associated the larger semicircle with the adsorbate capacitance (C_{film}) and adsorbate resistance (R_{film}).[27,69,70] However, C_{film} and R_{film} also refer to the TMO's surface defects and charge dynamics (i.e., density of states available to interact); therefore, it can further inform about limiting processes at the catalyst interface that are intrinsic properties of the material.[71] While C_{film} increases with aging, reflecting an increase in ECSA, R_{film} decreases due to different bondings in the NiOOH formed and the presence of charged species from the electrolyte in the hydrous layers. As noted by Alexandrov and Zagalskaya, the leaching of the dopants can affect the OER stability through the creation of defects.[72] The degree to which dopant leaching can influence the ECSA, as the catalyst is activated, is yet to be tested. If the

https://doi.org/10.1021/jacs.4c14493
J. Am. Chem. Soc. XXXX, XXX, XXX−XXX

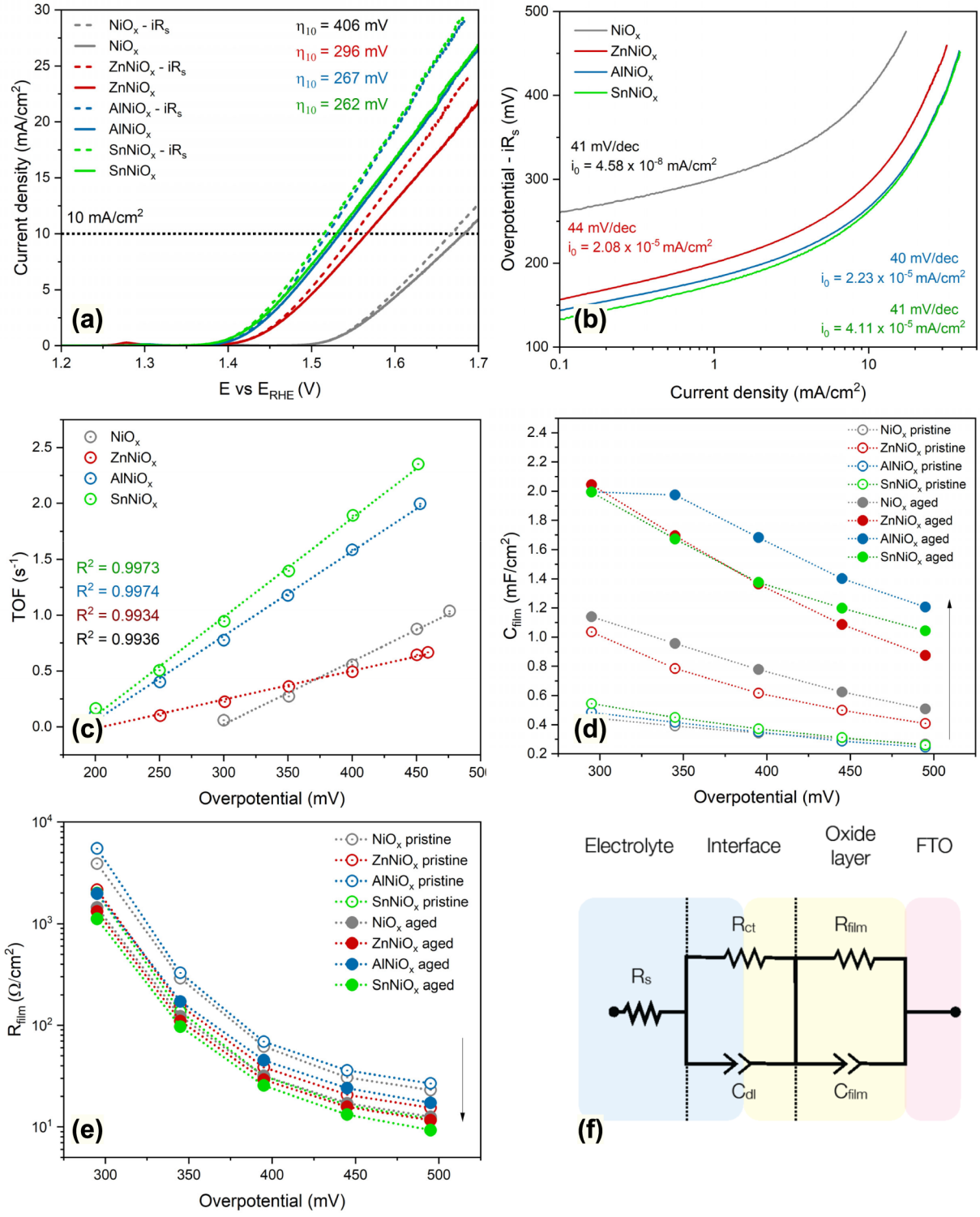

Figure 1. Catalytic performance plots: (a) LSV measured at 1 mV/s after 600 cycles of conditioning (*iR* drop correction of 1.5 Ω, (b) Tafel plot and analysis measured in the colored area (yellow), (c) TOF, (d) C_{film}, and (e) R_{film} as a function of applied potential before (open circle) and after (closed circle) conditioning, and (f) the equivalent circuit used to interpret the EIS.

leaching can enhance ECSA, it is expected that there is higher OER activity.

The best catalysts, $SnNiO_x$ and $AlNiO_x$, were the materials that presented the highest C_{film} (both $SnNiO_x$ and $AlNiO_x$) and the lowest R_{film} ($SnNiO_x$) after aging. The time constant τ for $AlNiO_x$ and $SnNiO_x$ appeared to be similar [as shown in the LSV in Figure 1a], but for different reasons; $AlNiO_x$ had the highest C_{film} followed by $SnNiO_x$, but $SnNiO_x$ had the lowest R_{film}, while $AlNiO_x$ had the highest R_{film} of all aged catalysts. This observation suggests that high C_{film} reflects stronger M−O adsorption due to positive charge buildup at the interface and since C_{film} reflects the density of states available to interact, which favors OER energetically. However, a low R_{film} is necessary to favor the charge transfer across SEI

https://doi.org/10.1021/jacs.4c14493
J. Am. Chem. Soc. XXXX, XXX, XXX−XXX

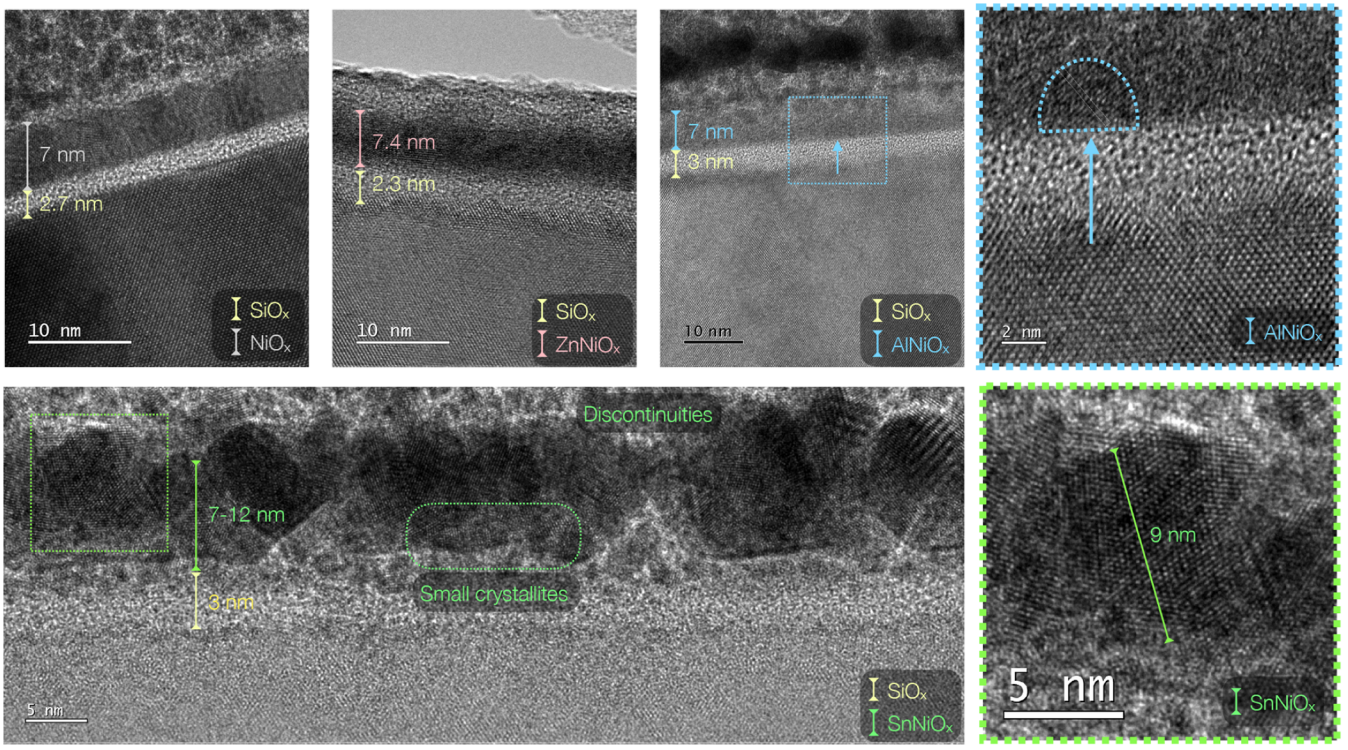

Figure 2. Film crystalline structure and morphology were obtained by FIB-TEM.

and speed up the OER kinetics. Thus, we hypothesize that the dopant is tuning the charge dynamics and mechanism by increasing the hole concentration and mobility in the valence band (high C_{film} leading to more DOS and strong adsorption) and high electron mobility in the conduction band (low R_{film} and high kinetic rate). Interestingly, the aged $SnNiO_x$ Bode Nyquist plots presented a diffusion feature toward higher frequency that required an additional Gerischer to optimize the circuit elements.[73−75] This feature is associated with the formation of vacancies of O_2 due to a chemical reaction involving the exchange of O_2 between the gas phase and $SnNiO_x$, which can indicate that the LOM is also occurring in $SnNiO_x$ and further supports the higher TOF observed.

The stability of the dopants in NiO_x can be understood in terms of the Pourbaix diagrams of ZnO, Al_2O_3, and SnO_4 in an alkaline environment and anodic potentials.[76] The Pourbaix diagram for these dopants in the potential region of the OER predicts that $ZnNiO_x$ and $AlNiO_x$ leach, while NiO_x and $SnNiO_x$ tend to passivate. Compared with pristine films, the ICP-MS of the aged films confirms that the highest dopant concentration losses follow $ZnNiO_x$ > $AlNiO_x$ > NiO_x > $SnNiO_x$. The stability of all metallic species can also be related to the flexibility in their oxidation states, which are rigid in Zn^{2+} and Al^{3+}, and reactions are driven by local pH gradients in each step of the OER mechanism, which is a similar process that happens in battery degradation.[77] To confirm the catalytic trends of TOF, the TON was measured with chronoamperometry at 400 mV overpotential for 1 h (Figure S16). The integrated charges over 1 h, which gave the TON, confirm the trend of catalytic activity going from highest to lowest in the order of $SnNiO_x$ (8.9), $AlNiO_x$ (5.8), NiO_x (2.4), and $ZnNiO_x$ (1.8). The largest activity loss observed in $AlNiO_x$ (36%) is due to transport limitations from the excess of bubbles instead of catalytic activity. The stability of $SnNiO_x$ was tested through 4 cycles of CP (1/1/12/1 h) held at 10 mA/cm^2 with a rest interval (Figure S18). $SnNiO_x$ presented high stability during prolonged CP (12 h) and signs of recovery (drop in overpotential) after the rest periods. This behavior in batteries is known as capacitive relaxation, but it has not been investigated in catalysts.[78]

Chemical Structure, Composition, and Morphology. The doped NiO_x recipes constituted 16 supercycles with a fixed 1:25 ratio of M^{n+}:NiO_x with a total of 400 cycles of Ni precursor pulse to control Ni metal loading in the nanofilms (Figure S1), and the frequency of the doping cycles to control free carrier density.[79] ICP-MS acid digestion and XPS provide qualitative estimates of TMO stoichiometry, showing that the metal loading and M^{n+}:NiO_x ratios vary and were higher than the supercycle ratio, confirming the difficulty in controlling the GPC for each different metal oxide containing Ni, Zn, Al, and Sn (Tables S7, S9, and S10). The dopant-to-Ni ratio in the different films, obtained by ICP-MS, was Zn^{2+}:Ni (39:61 in Si, 30:70 in FTO), Al^{3+}:Ni (34:66 in Si, 32:68 in FTO), and Sn^{4+}:Ni (26:74 in Si, 39:61 in FTO). XPS atomic ratios indicate that NiO_x in FTO and Si had a Ni:O ratio of 40:60, which confirms the p-type character with Ni vacancies.[42,80] All catalysts have similar oxygen content (i.e., 60%), indicating the p-type character of NiO_x does not change with doping. However, the concentration of dopants in FTO varies significantly: $AlNiO_x$ (20%), $ZnNiO_x$ (19%), and $SnNiO_x$ (5%). This can be related to difficulties in deposition control of binary oxides, which is challenging due to changes in surface chemistry and nucleation behavior during the supercycles, leading to growth rate variations and nonconstant growth-per-cycle (GPC).[29,79,81]

The results of GIXRD (Figure S21 and Table S6) show that the thin films are polycrystalline and have a face-centered cubic structure. The relatively broad peaks indicate that the films are composed of small crystallites of 2−3 nm, depending on the crystallite facet (Figure S23). Thermal ALD processes carried

https://doi.org/10.1021/jacs.4c14493
J. Am. Chem. Soc. XXXX, XXX, XXX−XXX

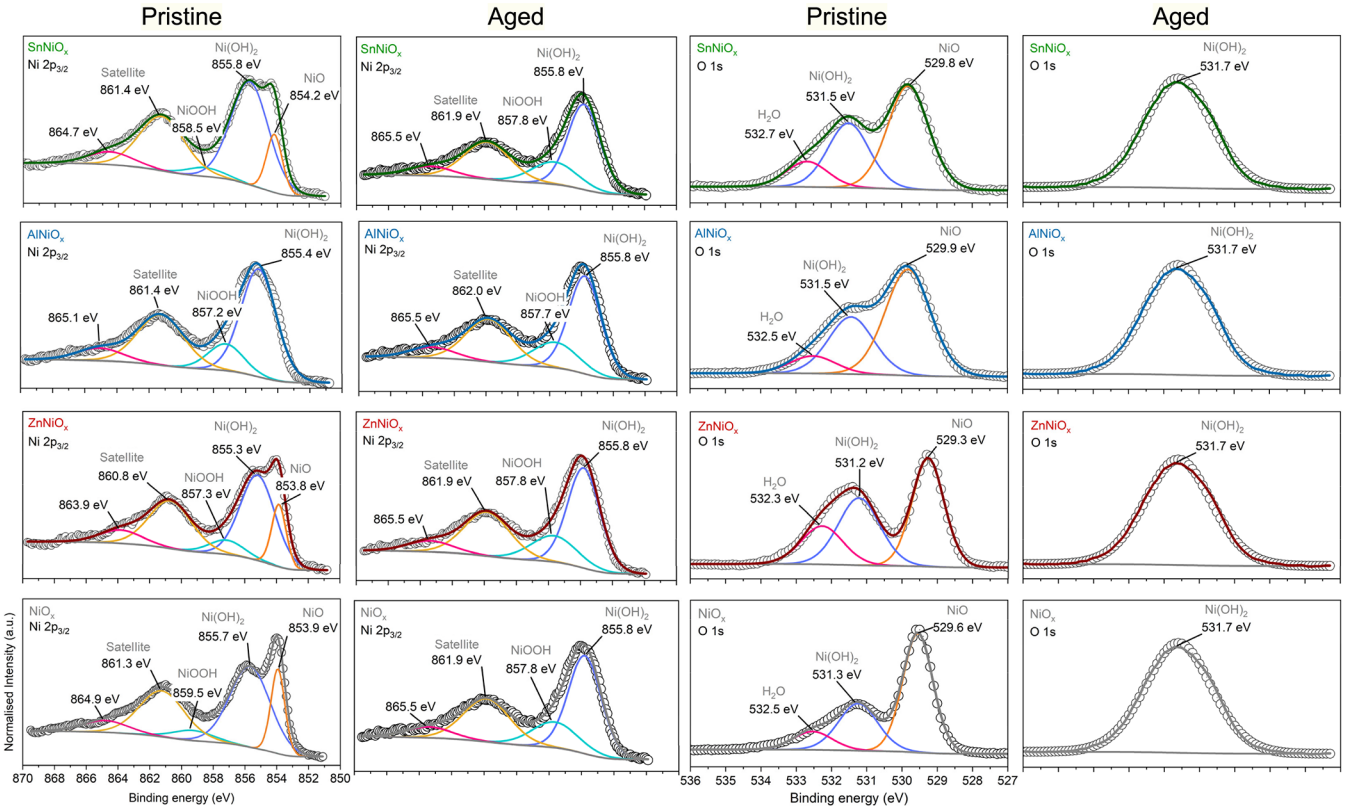

Figure 3. Ni 2p (columns 1 and 2) and O 1s (columns 3 and 4) peaks of XPS on FTO before (pristine) and after (aged) the OER. The main line colors represent NiO_x (gray), $ZnNiO_x$ (red), $AlNiO_x$ (blue), and $SnNiO_x$ (green). NiO (orange), $Ni(OH)_2$ (blue), and NiOOH (cyan) peak positions can be compared to the reference Ni^{3+} $2p_{2/3}$ peak at 855.6 eV in $LiNiO_2$.[84,86]

out at 150 °C result in amorphous films, but in PE-ALD, the high energy of the ion species interacting with the growth surface can induce crystallinity. Adding the different metal cations to NiO_x affects the lattice parameter (a) according to the size and quantity of the cations. $AlNiO_x$ (4.116 Å) reduces the lattice parameter a compared to NiO_x (4.218 Å), followed by $SnNiO_x$ (4.195 Å) and $ZnNiO_x$ (4.223 Å). Exceptionally, in the (111) plane direction, $SnNiO_x$ (4.250 Å) > $ZnNiO_x$ (4.246 Å). The peak broadening and smaller crystallite sizes of $SnNiO_x$ and $AlNiO_x$ suggest that their polycrystalline structures are more closely related to one another than those of $ZnNiO_x$ and NiO_x, which are also similar. Bent et al. reported that Al^{3+} contracts the NiO lattice due to the occupancy of Al^{3+} at the octahedral sites.[79] Their study also found that increased ratios of Al^{3+} composition in NiO_x substantially distorted the rocksalt structure, resulting in amorphous-like films.

The final thicknesses measured by ex-situ SE on the Si substrates were NiO_x (6.5 nm), $ZnNiO_x$ (8.5 nm), $AlNiO_x$ (7.0 nm), and $SnNiO_x$ (8.0 nm), and confirmed by FIB-TEM as shown in Figure 2. ToF-SIMS confirmed the thickness of the Si and FTO substrates (pristine and aged) and revealed the composition by analyzing the depth profile (Figures S19–S22). ToF-SIMS is not a common technique used to analyze catalysts, but it offers high surface sensitivity and low detection limits to analyze composition.[82] Changes in electrolyte ion concentration are observed in the structure of the aged films and very low [Fe] concentration in some films, as revealed by ToF-SIMS (Figures S19–S22). This unintentional [Fe], even below ppb level, can change the OER activity.[28] Thus, a future study should confirm that the trend of the OER remains using a purified KOH 99.99% electrolyte. AFM and SEM showed that the film morphologies are uniform in Si and FTO (Figures S24–S27). The roughness of the nanofilms mimics the roughness of the substrate in the Si wafer (R_s < 1 nm) and FTO (R_s ≈ 20 nm). The SEM image of the aged films shows the crystalline features of the formation of the NiO_x hydroxides, indicated by needle-like white lines.

XPS before and after the OER shows the changes that occur when the pristine film transforms into the active NiOOH catalyst, as illustrated by the Ni $2p_{3/2}$ and O 1s spectra in Figure 3. The XPS peak fitting can be found in Tables S9 and S10, and Figures S28–S35. The Ni 2p peak can be described by satellite peaks, multiplet splitting, and screening mechanisms that can be deconvoluted into multiple other peaks.[83−85] For the sake of simplicity, the Ni $2p_{3/2}$ peaks were deconvoluted into three main peaks at 853.9, 855.7, and 859.5 eV, associated with NiO (orange), $Ni(OH)_2$ (blue), and NiOOH (cyan), respectively, as compared to a reference Ni^{3+} peak in $LiNiO_2$ (855.6 eV).[86] McIntyre et al. showed that the free ion multiplet envelopes for Ni^{2+} and Ni^{3+} produce the main line and satellite structures for $Ni(OH)_2$ and NiOOH, as shown in Figure 3.[84] Three peaks were used to describe the O 1s peak located at 529.6 (M−O, orange), 531.3 (M−OH or O_2^- defect, blue), and 532.5 eV (adsorbed H_2O, pink). After conditioning, the aged catalysts present XPS features that confirm the transformation to metal hydroxide species, potentially the β-NiOOH.[83,87,88] This is evident by the $Ni(OH)_2$ $2p_{2/3}$ peak shift to 855.8 eV and O 1s (M−OH) to 531.7 eV, combined with the disappearance of the NiO $2p_{2/3}$ and O 1s (M−O) at lower binding energies. The XPS of the aged catalysts suggests that the OER activity of the active

https://doi.org/10.1021/jacs.4c14493
J. Am. Chem. Soc. XXXX, XXX, XXX−XXX

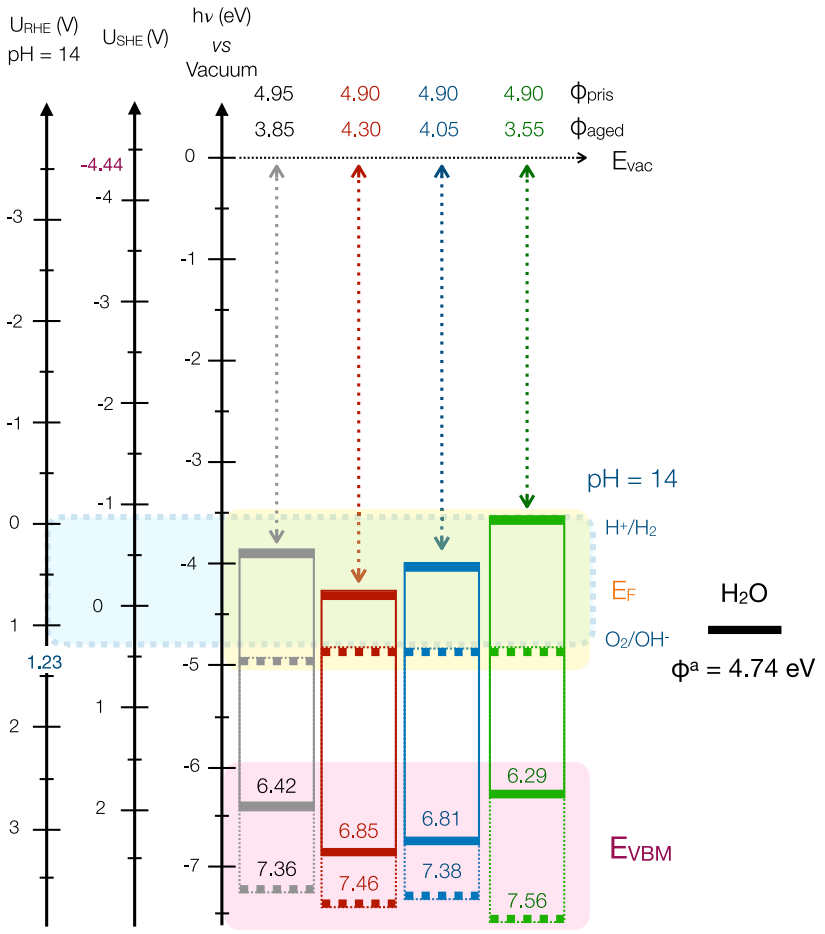

Figure 4. Band structure diagram reconstructed from the UPS measured in FTO before (dashed) and after (line) the OER. ϕ = work function, IE = ionization potential, VBM = valence band maximum, CBM = conduction band minimum, and E_F = Fermi level. The energy axis was shifted to negative values for convenience, and the potential values and water ϕ were taken from the literature.[90,91]

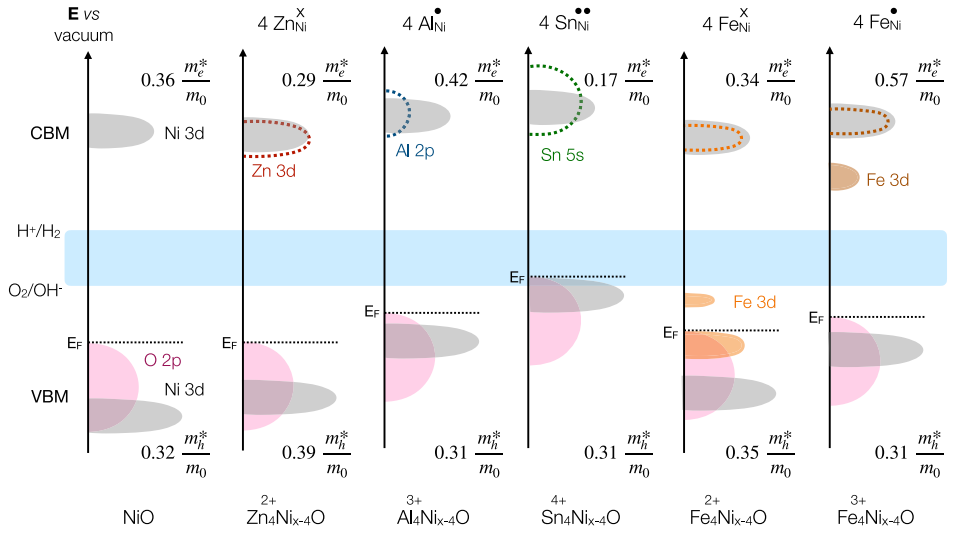

Figure 5. Band structure diagram of NiO and doped NiO reconstructed from integrated DOS, and charge carrier effective masses. Ni 3*d* (gray), O 2*p* (pink), Zn 3*d* (red), Al 2*p* (blue), Sn 5*s* (green), Fe 3*d* (orange). The Kröger−Vink notation at the top indicates substitutional defect charges. Energy scale relation to water-splitting (blue) E_{RHE} potentials according to the literature.[90]

catalysts should be identical or change as a function of the concentration of $Ni(OH)_2$. However, the peaks of the M dopants before and after the OER (Figure S18) show that aged Sn^{4+} is the only dopant with a significant oxidation peak shift (ΔE_{peak} = 1.2 eV), indicating that Sn^{4+} in $SnNiO_x$ acts in collaboration with Ni^{3+}.

https://doi.org/10.1021/jacs.4c14493
J. Am. Chem. Soc. XXXX, XXX, XXX−XXX

The diagram in Figure 4 shows the UPS reconstructed band diagram [E_F (yellow) and VBM (pink)] aligned with energy values (taken as negative for convenience) and relevant potentials, shifted with respect to the vacuum level, to compare energy values with the relevant OER potential region (blue). The E_F and VBM are shown before (dashed) and after (line) the OER. The UPS spectra can be found in Figures S36 and S37. During the OER, as indicated by the potential axis, the VBM and E_F are shifted downward. Because the adsorption occurs through holes in the VBM, or nonbonding defect states, the position of the VBM determines how strong the adsorption is, i.e., the larger the difference, the stronger the interaction. The E_F, as defined by Wolkenstein, acts as a regulator of the VBM and CBM in each step of the reaction because the creation of holes in the valence band depends on the catalyst's ability to lose electrons through the applied bias. The final E_F position, which has shifted upward, has a similar trend to the intrinsic catalytic activity, with $SnNiO_x$ being the best catalyst and highest E_F, except that NiO_x and $AlNiO_x$ are very similar, with the latter final VBM of $AlNiO_x$ lying below NiO_x. Similarly, Erbe et al. investigated in situ operando surface oxide formation in Cu during the OER and detected that oxides formed (CuO, Cu_2O, and Cu_4O_3) after the OER were all n-type rather than p-type as predicted.[89] The significant changes in E_F observed here serve as a probe to support the need for in situ operando experiments that can monitor electronic properties with the precision offered by UPS.

Electrostatic and Electronic Properties. The diagram in Figure 5 illustrates the integrated DOS and the calculated VBM and CBM charge carrier effective masses from the band diagram for NiO and doped NiO (Figures S41 and S42), relative to the water-splitting E_{RHE} potentials.[90] The addition of the different M dopants not only upshifts the Ni 3*d* orbital in the VB, reaching the VBM in $Sn_4^{4+}Ni_{x-4}O$ but also changes hole mobility, with the lowest value of 0.31 hole effective mass in $Al_4^{3+}Ni_{x-4}O$, $Sn_4^{4+}Ni_{x-4}O$, and $Fe_4^{3+}Ni_{x-4}O$. Furthermore, resonant dopant defect levels appear in the CBM (Figure S40), and the electron mobility increased significantly in $Sn_4^{4+}Ni_{x-4}O$ (lowest electron effective mass). This result is easily understood by the significantly dispersed Sn 5s orbital, improving electron conductivity as confirmed by EIS. Thus, high hole and electron mobility in $SnNiO_x$ supports the best OER activity. Adding n-type Zn^{2+} flattens the VBM (see Figure S39), which decreases hole mobility and somewhat improves electron conductivity. Knowing that $ZnNiO_x$ has the lowest level of OER activity can indicate that hole mobility can be more relevant to OER catalysis than electron conductivity. Even though p-type Al^{3+} improves hole mobility, it decreases electron mobility, as seen in the EIS R_{film} measurements. Because $AlNiO_x$ has the second-best OER activity after $SnNiO_x$, it also supports that hole mobility is more important to promote the OER than electron mobility. To understand how the defects affect carrier concentration relative to the chemical potentials of the materials would require a thermoelectric transport property study, which is beyond the scope of this work. The energetic role of the dopants in promoting the OER activity can be interpreted by how the E_F position is shifted relative to the OER potentials. As noted by Liu et al., the observed upshift in E_F by the addition of Al^{3+}, Sn^{4+}, and Fe^{3+} to NiO, in contrast to Zn^{2+} and Fe^{2+}, is predicted to improve OER activity by reducing the number of electrons in antiorbitals, thus strengthening the binding of the OER oxygen intermediate species (Figure 5).[92] This can also be viewed indirectly by how the dopant strengthens the Ni−O bonding (shorter bond lengths, higher electronegativity, and covalency), such that the length decreases in the order of NiO (2.08 Å), $Zn_4^{2+}Ni_{x-4}O$ (2.08 Å), $Al_4^{3+}Ni_{x-4}O$ (2.04 Å), $Sn_4^{4+}Ni_{x-4}O$ (1.97 Å), $Fe_4^{2+}Ni_{x-4}O$ (2.07 Å), and $Fe_4^{3+}Ni_{x-4}O$ (2.02 Å).

The diagram in Figure 5 can partially explain the Fe-induced OER promotion.[93] It is known that the addition of approximately 25% of Fe into NiO_x introduces the signature of the Fe_2O_3 spinel structure with mixed Fe^{2+} and Fe^{3+} oxidation states and promotes the OER.[30,94] In Figure 5, this would be characterized by a mixture of $Fe_4^{2+}Ni_{x-4}O$ and $Fe_4^{3+}Ni_{x-4}O$ DOS, which has two effects: (i) the Ni 3*d* orbital upshift in Fe^{3+} (as discussed), and (ii) the appearance of midgap shallow defect states (nonbonding states), which are known to promote the OER in Fe_2O_3.[95] Furthermore, ferromagnetism and ferroelectricity are likely to play a role in the OER, and this certainly needs to be explored.[96] Herein, we observe that the Fe dopant is the only open-shell metal dopant with a magnetic dipole moment (μ_B) and varying spin states depending on the M oxidation state (Fe^{2+} $3d^6$ and Fe^{3+} $3d^5$), which alters the spin density of the O atoms in $Fe_1^{2+}Ni_{x-1}O$, thus leading to a highly spin-polarized and correlated material (Figure S39).

Several OER descriptors have been investigated, with the d-band center from Nørskov et al. being the most popular to describe structure−activity relationships in transition metals.[39,97,98] In TMOs, reactivity must be related to the physical nature of the TM−O chemical bond and can be associated with properties related to electronegativity, 3d orbitals, and oxophilicity.[99] In the case of the p-type NiO_x, the VBM is composed of O 2*p* and Ni 3*d* orbitals, both of which are very localized, with the former being the most, and for this reason, NiO_x has low hole conductivity.[80] Thus, shifting the position of the 3*d* orbital relative to the 2*p* can improve hole semiconductivity in NiO_x, since it places the metal orbital at the VBM, and this can be achieved by doping.[100] This shift in the 3*d* orbital energy level relative to the O 2*p* can also change the overall energy position of the VBM and the Fermi level of NiO_x, as observed experimentally in this work. As shown by Liu et al., the energy of the VBM *d*-states relative to the E_F can be used as a descriptor to probe the electronic origin of the OER surface reactivity.[92] Thus, the hole density in the catalyst VBM acts as active sites for the OER, and the flux of electrons by the CBM maintains the creation of holes aided by the applied positive bias. Hence, the role of the dopant in improving the electron conductivity is also essential.

Figure S43 compares (a) the induced dipole moment ($\Delta p_z = p_{field} - p_{slab}$) when a finite high-energy field (5.14×10^{11} V/m) was applied in the nonperiodic direction (z) of the slabs, and (b) the average of the diagonal of the α_e tensor when a low-energy field (5.14×10^{-04} V/m) is applied in the slabs' x, y, and z directions. The general trend in Δp_z [Figure S43a] increases when the surface is charged. The exception of $Al_1Ni_{x-1}O$ and $Al_1^{3+}Ni_{x-1}O$ can be due to the electronic configuration of the neutral Al defect being $[3s^23p^1]$ versus in $Al_1^{3+}Ni_{x-1}O$ is $[3s^23p^0]$. The α_e [Figure S43b] increases when one electron is removed from the VBM in $Ni_{Ni}^{\bullet}$, $Al_{Ni}^{\bullet}$, $Sn_{Ni}^{\bullet\bullet}$, and $Fe_{Ni}^{\bullet}$, and decreases when the second electron is removed in

https://doi.org/10.1021/jacs.4c14493
J. Am. Chem. Soc. XXXX, XXX, XXX−XXX

$Ni_{Ni}^{\bullet\bullet}$ and $Fe_{Ni}^{\bullet\bullet}$. This suggests higher oxidation states in the 3d orbitals of NiO and $Fe_1Ni_{x-1}O$ localized the positive charge states. Adding $Sn_{Ni}^{\bullet\bullet}$ into NiO leads to the highest α_e, which can be attributed to the positive charge residing in the larger $5s^25p^0$ orbitals. The low α_e values found in the neutral slabs, i.e., NiO, $Zn_{Ni}^{\times}$, $Al_{Ni}^{\times}$, $Sn_{Ni}^{\times}$ and $Fe_{Ni}^{\times}$, in contrast to the charged ones, are due to the larger Δp in the charged slabs. Overall, the α_e values have a similar OER activity trend of $Zn_{Ni}^{\times}$ < NiO (or charged defects) < $Al_{Ni}^{\bullet}$ < $Sn_{Ni}^{\bullet\bullet}$. The α_e does not correlate with the Fe effect discussed; that is, adding Fe to NiO does not result in the highest α_e values, supporting the idea that the promotion of the OER in Fe-NiO is not of electrostatic origin. The relationship between electronegativity, chemical hardness, and softness with the chemical capacitance C_μ (i.e., surface DOS) has been defined in the work of Bueno et al.[101−103] These properties can be associated with the electric polarizability (α_e) of the catalysts, which is a reactivity descriptor in enzyme catalysis and host−guest interaction in supramolecular chemistry, which can be experimentally measured.[104−107]

The electrostatic potential maps (EPMs) in Figure 6 illustrate how electrons are distributed on the isosurface of

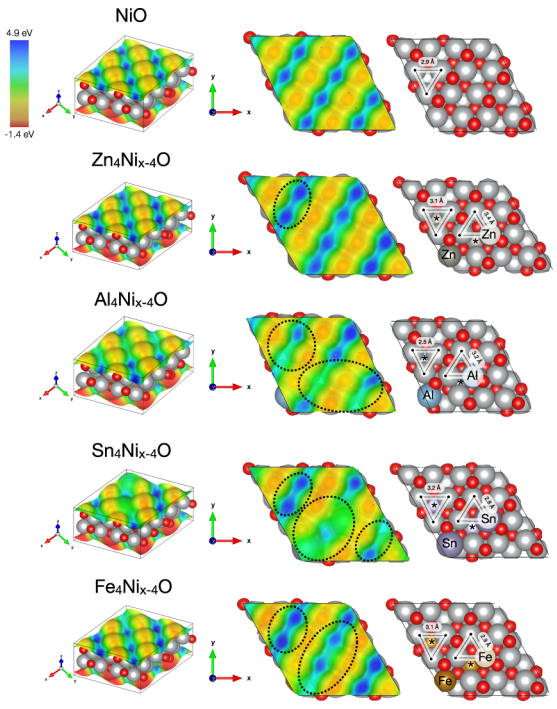

Figure 6. Local electrostatic potential maps of NiO and neutral defect slabs $Zn_1Ni_{x-1}O$, $Al_1Ni_{x-1}O$, $Sn_1Ni_{x-1}O$, and $Fe_1Ni_{x-1}O$ colored according to the energy values of electron density isosurface (0.0005 au cutoff). Strong electrostatic interactions are related to the electron-rich regions (red) and electron-poor regions (blue) and weaker VdW-like in intermediate regions (green). Perspective view (left), top view (middle), and slab top view (right).

the electron density of the optimized slab structures and can be used as local reactivity descriptors of active sites.[108] The surface colors indicate regions of electron accumulation (red) and electron depletion (blue), which tend to have strong electrostatic interactions. In the right part of Figure 6, bond lengths indicate how the M−O bonding changes and how that influences the charge distribution. The dashed circles in Figure 6 represent the changes in charge distribution due to the addition of the dopants. $Zn_1Ni_{x-1}O$, $Sn_1Ni_{x-1}O$, and $Fe_1Ni_{x-1}O$ have a slight increase in the blue region (top left of the top view), and $Al_1Ni_{x-1}O$ has a decrease. These EPM changes correspond to an increase in the bond lengths in $Zn_1Ni_{x-1}O$, $Sn_1Ni_{x-1}O$, and $Fe_1Ni_{x-1}O$, and a reduction in $Al_1Ni_{x-1}O$ compared to NiO (top view of the slabs). The same trend is found in the other circled regions, indicating that shorter M−O bonds have a higher electron density. Because the OER catalysts act as electron acceptors, active sites should be blue and green regions. Interestingly, $Al_1Ni_{x-1}O$ and $Sn_1Ni_{x-1}O$ have more zones associated with weaker electrostatic interactions (green) when compared to $Zn_1Ni_{x-1}O$.

The surface reactivity was tested by water dissociative adsorption energy (E_{WD}) (Table 2). The details for choosing

Table 2. Single Site Water Dissociative Adsorption Energy E_{WD} in the hpc Site of NiO and Doped NiO (111) Oxygen Terminated Surfaces

Catalyst	Defect	E_{WD} (eV)
NiO	−	−3.90
$Zn_1Ni_{x-1}O$	$Zn_{Ni}^{\times}$	−3.85
$Al_1Ni_{x-1}O$	$Al_{Ni}^{\times}$	−4.13
$Al_1Ni_{x-1}O$	$Al_{Ni}^{\bullet}$	−5.10
$Sn_1Ni_{x-1}O$	$Sn_{Ni}^{\times}$	−3.68
$Sn_1Ni_{x-1}O$	$Sn_{Ni}^{\bullet\bullet}$	−5.48
$Fe_1Ni_{x-1}O$	$Fe_{Ni}^{\times}$	−4.28
$Fe_1Ni_{x-1}O$	$Fe_{Ni}^{\bullet}$	−4.72
$Fe_1Ni_{x-1}O$	$Fe_{Ni}^{\bullet\bullet}$	−6.25

the NiO (111) oxygen-terminated facet and specific active site (hollow face-centered) can be found in the Supporting Information. The results in Table 2 show that H_2O dissociation is favored on the charged surfaces ($Al_{Ni}^{\bullet}$, $Sn_{Ni}^{\bullet\bullet}$, $Fe_{Ni}^{\bullet}$, and $Fe_{Ni}^{\bullet\bullet}$) when compared to the neutral surfaces (NiO_x, $Zn_{Ni}^{\times}$, $Al_{Ni}^{\times}$, $Sn_{Ni}^{\times}$, and $Fe_{Ni}^{\times}$). This is expected as a result of stronger electrostatic interactions between the charged surfaces. Comparing the E_{WD} values for the neutral slabs, the trend in reactivity increases in the order of $Zn_{Ni}^{\times}$ < $Sn_{Ni}^{\times}$ < $Al_{Ni}^{\times}$ < $Fe_{Ni}^{\times}$. In charged slabs, the E_{WD} reactivity increases in the order of $Fe_{Ni}^{\bullet}$ < $Al_{Ni}^{\bullet}$ < $Sn_{Ni}^{\bullet\bullet}$ < $Fe_{Ni}^{\bullet\bullet}$. The E_{WD} for neutral and charged surfaces has a similar trend to the observed OER activity ($ZnNiO_x$ < NiO_x < $AlNiO_x$, $SnNiO_x$) and predicts that doping NiO with Fe^{n+} improves surface reactivity in the neutral $Fe_{Ni}^{\times}$ and charged $Fe_{Ni}^{\bullet\bullet}$ defects compared to other surfaces with the same charge state. As a general remark on the reactivity trend, it seems that when Al^{3+}, Sn^{4+}, and Fe^{2+} (or higher oxidation states) are added into NiO, a combination of electronic and electrostatic effects increases the interaction (higher stabilization) with H_2O; thus, one can expect a similar trend when these surfaces interact with other OER oxygen intermediate species. Further insight into the electrostatic and orbital energy components that can explain this reaction can be obtained through energy decomposition analysis, which is beyond the scope of this work.[109]

https://doi.org/10.1021/jacs.4c14493
J. Am. Chem. Soc. XXXX, XXX, XXX−XXX

CONCLUDING REMARKS AND OUTLOOK

We studied the electrochemical activity of the OER in self-supported nanofilm catalysts (NiO_x, $ZnNiO_x$, $AlNiO_x$, and $SnNiO_x$) produced with plasma-enhanced atomic layer deposition (PE-ALD) on an inert substrate (FTO). The nanofilms showed great stability, durability, and high activity even after conditioning for several cyclic voltammetry (CV) cycles at slow scan rates (600 cycles at 20 mV/s). The order found in the OER activity was $ZnNiO_x$ < NiO_x < $AlNiO_x$ < $SnNiO_x$. A future study should investigate whether different Sn^{4+} concentrations can enhance the OER activity. All catalysts presented a first-order mechanism, as indicated by Tafel analysis. Our results suggest that the enhancement of the OER activity arises from a balance between optimal Fermi level positioning (E_F), hole concentration and mobility, and low charge resistance (R_{film}). DFT modeling supports the hypothesis that two effects tune the NiO_x intrinsic activity. The first is the electrostatic charge effect arising from the oxidation state of the M^{n+} dopant that supports a higher concentration of positive charge at the solid−electrolyte interface (associated with C_{film}). The second is a high charge delocalization that results from M^{n+}-NiO_x orbital mixing (associated with R_{film}) and allows the excess charge to flow. Our results support the idea that the promotion of the OER in NiO_x by adding an M dopant occurs via balancing electrostatic (positive charge accumulation) and electronic (orbital charge delocalization) effects. This study contributes to future experimental and theoretical developments of optimized electrochemical catalysts by informing that the OER activity of NiO_x is improved with M^{n+} dopants with higher oxidation states and larger delocalized orbitals.

ASSOCIATED CONTENT

Supporting Information

The Supporting Information is available free of charge at https://pubs.acs.org/doi/10.1021/jacs.4c14493.

Detailed experimental ALD materials and procedures, electrochemical results, chemical structure, composition, and morphology characterization, and DFT calculations (PDF)

AUTHOR INFORMATION

Corresponding Author

Bram Hoex − *School of Photovoltaic and Renewable Energy Engineering, University of New South Wales, Kensington, NSW 2052, Australia;* orcid.org/0000-0002-2723-5286; Email: b.hoex@unsw.edu.au

Authors

Ina Østrøm − *School of Photovoltaic and Renewable Energy Engineering, University of New South Wales, Kensington, NSW 2052, Australia;* orcid.org/0000-0001-7159-2574

Marco Favaro − *Institute for Solar Fuels, Helmholtz-Zentrum Berlin für Materialien und Energie GmbH, Berlin 14109, Germany;* orcid.org/0000-0002-3502-8332

Moein Seyfouri − *UNSW, Kensington, NSW 2052, Australia*

Patrick Burr − *School of Mechanical and Manufacturing Engineering, University of New South Wales, Kensington, NSW 2052, Australia;* orcid.org/0000-0003-4796-9110

Complete contact information is available at: https://pubs.acs.org/10.1021/jacs.4c14493

Author Contributions

All authors discussed the results and contributed to reviewing and editing the manuscript.

Notes

The authors declare no competing financial interest.

ACKNOWLEDGMENTS

IØ thanks the University of New South Wales (UNSW) for a Scientia PhD Scholarship [RPR00131447]. This work was partially supported by the Helmholtz Energy Materials Foundry (HEMF, GZ 714-48172-21/1), funded by the German Federal Ministry of Education and Research (BMBF). This research was undertaken with the assistance of resources and services from the National Computational Infrastructure, which the Australian Government supports. We thank everyone involved in the UNSW-NCI partner trial scheme; the Multimodal Australian ScienceS Imaging and Visualisation Environment (MASSIVE); the Pawsey Supercomputing Centre, which is supported by the Australian Government and the Government of Western Australia; and was enabled by Intersect Australia Limited. Learn more at www.intersect.org.au. The authors also thank J. Hart and A. Hossain for the scientific discussions and Prof. C. Zhao and S. Wang for the initial electrochemical testing. Special thanks to the Mark Wainwright Analytical Centre, including B. Gong and S. Yin from the Solid State Elemental Analysis Unit of the Surface Analysis Laboratory, and R. Webster and Y. Yao from the Electron Microscope Unit.

REFERENCES

(1) Chen, F.-Y.; Wu, Z.-Y.; Adler, Z.; Wang, H. Stability Challenges of Electrocatalytic Oxygen Evolution Reaction: From Mechanistic Understanding to Reactor Design. *Joule* **2021**, *5*, 1704−1731.

(2) Yu, Z.-Y.; Duan, Y.; Feng, X.-Y.; Yu, X.; Gao, M.-R.; Yu, S.-H. Clean and Affordable Hydrogen Fuel from Alkaline Water Splitting: Past, Recent Progress, and Future Prospects. *Adv. Mater.* **2021**, *33* (31), 2007100.

(3) Kou, T.; Wang, S.; Li, Y. Perspective on High-Rate Alkaline Water Splitting. *ACS Mater. Lett.* **2021**, *3*, 224−234.

(4) You, B.; Sun, Y. Innovative Strategies for Electrocatalytic Water Splitting. *Acc. Chem. Res* **2018**, *51*, 1571−1580.

(5) Yoshino, S.; Takayama, T.; Yamaguchi, Y.; Iwase, A.; Kudo, A. CO_2 Reduction Using Water as an Electron Donor over Heterogeneous Photocatalysts Aiming at Artificial Photosynthesis. *Acc. Chem. Res.* **2022**, *55*, 966−977.

(6) Chebrolu, V. T.; Jang, D.; Rani, G. M.; Lim, C.; Yong, K.; Kim, W. B. Overview of Emerging Catalytic Materials for Electrochemical Green Ammonia Synthesis and Process. *Carbon Energy.* **2023**, *5* (12), No. e361.

(7) Jesudass, S. C.; Surendran, S.; Kim, J. Y.; An, T.-Y.; Janani, G.; Kim, T.-H.; Kim, J. K.; Sim, U. Pathways of the Electrochemical Nitrogen Reduction Reaction: From Ammonia Synthesis to Metal-N_2 Batteries. *Electrochem. Energy Rev.* **2023**, *6* (1), 27.

(8) Katsounaros, I.; Cherevko, S.; Zeradjanin, A. R.; Mayrhofer, K. J. J. Oxygen Electrochemistry as a Cornerstone for Sustainable Energy Conversion. *Angew. Chem., Int. Ed.* **2014**, *53*, 102−121.

(9) Tahir, M.; Pan, L.; Idrees, F.; Zhang, X.; Wang, L.; Zou, J.-J.; Wang, Z. L. Electrocatalytic Oxygen Evolution Reaction for Energy Conversion and Storage: A Comprehensive Review. *Nano Energy.* **2017**, *37*, 136−157.

(10) Fabbri, E.; Schmidt, T. J. Oxygen Evolution Reaction - The Enigma in Water Electrolysis. *ACS Catal* **2018**, *8*, 9765−9774.

(11) Yu, M.; Budiyanto, E.; Tüysüz, H. Principles of Water Electrolysis and Recent Progress in Cobalt-, Nickel-, and Iron-Based Oxides for the Oxygen Evolution Reaction. *Angew. Chem., Int. Ed.* **2022**, *61* (1), No. e202103824.

(12) Seh, Z. W.; Kibsgaard, J.; Dickens, C. F.; Chorkendorff, I.; Nørskov, J. K.; Jaramillo, T. F. Combining Theory and Experiment in Electrocatalysis: Insights into Materials Design. *Science* **2017**, *355*, No. eaad4998.
(13) Li, W.; Shi, J.; Zhang, K. H. L.; MacManus-Driscoll, J. L. Defects in Complex Oxide Thin Films for Electronics and Energy Applications: Challenges and Opportunities. *Mater. Horiz.* **2020**, *7*, 2832−2859.
(14) Song, F.; Bai, L.; Moysiadou, A.; Lee, S.; Hu, C.; Liardet, L.; Hu, X. Transition Metal Oxides as Electrocatalysts for the Oxygen Evolution Reaction in Alkaline Solutions: An Application-Inspired Renaissance. *J. Am. Chem. Soc.* **2018**, *140*, 7748−7759.
(15) Song, J.; Wei, C.; Huang, Z.-F.; Liu, C.; Zeng, L.; Wang, X.; Xu, Z. J. A Review on Fundamentals for Designing Oxygen Evolution Electrocatalysts. *Chem. Soc. Rev.* **2020**, *49*, 2196−2214.
(16) Zhang, J.; Tao, H. B.; Kuang, M.; Yang, H. B.; Cai, W.; Yan, Q.; Mao, Q.; Liu, B. Advances in Thermodynamic-Kinetic Model for Analyzing the Oxygen Evolution Reaction. *ACS Catal.* **2020**, *10*, 8597−8610.
(17) Vij, V.; Sultan, S.; Harzandi, A. M.; Meena, A.; Tiwari, J. N.; Lee, W.-G.; Yoon, T.; Kim, K. S. Nickel-Based Electrocatalysts for Energy-Related Applications: Oxygen Reduction, Oxygen Evolution, and Hydrogen Evolution Reactions. *ACS Catal.* **2017**, *7*, 7196−7225.
(18) McCrory, C. C. L.; Jung, S.; Peters, J. C.; Jaramillo, T. F. Benchmarking Heterogeneous Electrocatalysts for the Oxygen Evolution Reaction. *J. Am. Chem. Soc.* **2013**, *135*, 16977−16987.
(19) Akbashev, A. R. Electrocatalysis Goes Nuts. *ACS Catal.* **2022**, *12*, 4296−4301.
(20) Anantharaj, S.; Noda, S. Dos and Don'ts in Screening Water Splitting Electrocatalysts. *Energy Adv.* **2022**, *1*, 511−523.
(21) Yang, H.; Driess, M.; Menezes, P. W. Self-Supported Electrocatalysts for Practical Water Electrolysis. *Adv. Energy Mater.* **2021**, *11* (39), 2102074.
(22) Timoshenko, J.; Cuenya, B. R. In-situ Operando Electrocatalyst Characterization by X-ray Absorption Spectroscopy. *Chem. Rev.* **2020**, *121* (2), 882−961.
(23) Lunger, J. R.; Karaguesian, J.; Chun, H.; Peng, J.; Tseo, Y.; Shan, C. H.; Han, B.; Shao-Horn, Y.; Gómez-Bombarelli, R. Towards Atom-Level Understanding of Metal Oxide Catalysts for the Oxygen Evolution Reaction with Machine Learning. *Npj Comput. Mater.* **2024**, *10* (1), 80.
(24) Soriano-López, J.; Schmitt, W.; García-Melchor, M. Computational Modelling of Water Oxidation Catalysts. *Curr. Opin. Electrochem.* **2018**, *7*, 22−30.
(25) Diaz-Morales, O.; Ledezma-Yanez, I.; Koper, M. T. M.; Calle-Vallejo, F. Guidelines for the Rational Design of Ni-Based Double Hydroxide Electrocatalysts for the Oxygen Evolution Reaction. *ACS Catal.* **2015**, *5*, 5380−5387.
(26) Østrøm, I.; Hossain, M. A.; Burr, P. A.; Hart, J. N.; Hoex, B. Designing 3d Metal Oxides: Selecting Optimal Density Functionals for Strongly Correlated Materials. *Phys. Chem. Chem. Phys.* **2022**, *24*, 14119−14139.
(27) Haghverdi Khamene, S.; van Helvoirt, C.; Tsampas, M. N.; Creatore, M. Electrochemical Activation of Atomic-Layer-Deposited Nickel Oxide for Water Oxidation. *J. Phys. Chem. C* **2023**, *127*, 22570−22582.
(28) Trotochaud, L.; Young, S. L.; Ranney, J. K.; Boettcher, S. W. Nickel−Iron Oxyhydroxide Oxygen-Evolution Electrocatalysts: The Role of Intentional and Incidental Iron Incorporation. *J. Am. Chem. Soc.* **2014**, *136*, 6744−6753.
(29) Baker, J. G.; Schneider, J. R.; Garrido Torres, J. A.; Singh, J. A.; Mackus, A. J. M.; Bajdich, M.; Bent, S. F. The Role of Aluminum in Promoting Ni−Fe−OOH Electrocatalysts for the Oxygen Evolution Reaction. *ACS Appl. Energy Mater.* **2019**, *2*, 3488−3499.
(30) Bucci, A.; García-Tecedor, M.; Corby, S.; Rao, R. R.; Martin-Diaconescu, V.; Oropeza, F. E.; de la Peña O'Shea, V. A.; Durrant, J. R.; Giménez, S.; Lloret-Fillol, J. Self-Supported Ultra-Active NiO-Based Electrocatalysts for the Oxygen Evolution Reaction by Solution Combustion. *J. Mater. Chem. A* **2021**, *9* (21), 12700−12710.
(31) Favaro, M.; Jeong, B.; Ross, P. N.; Yano, J.; Hussain, Z.; Liu, Z.; Crumlin, E. J. Unravelling the Electrochemical Double Layer by Direct Probing of the Solid/Liquid Interface. *Nat. Commun.* **2016**, *7* (1), 12695.
(32) Favaro, M.; Yang, J.; Nappini, S.; Magnano, E.; Toma, F. M.; Crumlin, E. J.; Yano, J.; Sharp, I. D. Understanding the Oxygen Evolution Reaction Mechanism on CoO_x using Operando Ambient-Pressure X-ray Photoelectron Spectroscopy. *J. Am. Chem. Soc.* **2017**, *139*, 8960−8970.
(33) Favaro, M.; Drisdell, W. S.; Marcus, M. A.; Gregoire, J. M.; Crumlin, E. J.; Haber, J. A.; Yano, J. An Operando Investigation of (Ni-Fe-Co-Ce)O_x System as Highly Efficient Electrocatalyst for Oxygen Evolution Reaction. *ACS Catal.* **2017**, *7*, 1248−1258.
(34) Man, I. C.; Su, H.; Calle-Vallejo, F.; Hansen, H. A.; Martínez, J. I.; Inoglu, N. G.; Kitchin, J.; Jaramillo, T. F.; Nørskov, J. K.; Rossmeisl, J. Universality in Oxygen Evolution Electrocatalysis on Oxide Surfaces. *ChemCatchem* **2011**, *3*, 1159−1165.
(35) Dickens, C. F.; Kirk, C.; Nørskov, J. K. Insights into the Electrochemical Oxygen Evolution Reaction with Ab Initio Calculations and Microkinetic Modeling: Beyond the Limiting Potential Volcano. *J. Phys. Chem. C* **2019**, *123*, 18960−18977.
(36) Yang, S.; Han, J.; Zhang, W. Proton-Coupled Electron Transfer in Electrocatalytic Water Splitting. *Chem. − Eur. J.* **2023**, *29* (69), No. e202302770.
(37) Warburton, R. E.; Soudackov, A. V.; Hammes-Schiffer, S. Theoretical Modeling of Electrochemical Proton-Coupled Electron Transfer. *Chem. Rev.* **2022**, *122*, 10599−10650.
(38) Xu, H.; Qi, J.; Zhang, Y.; Liu, H.; Hu, L.; Feng, M.; Lü, W. Magnetic Field-Enhanced Oxygen Evolution Reaction via the Tuneability of Spin Polarization in a Half-Metal Catalyst. *ACS Appl. Mater. Interfaces* **2023**, *15*, 32320−32328.
(39) Hong, W. T.; Welsch, R. E.; Shao-Horn, Y. Descriptors of Oxygen-Evolution Activity for Oxides: A Statistical Evaluation. *J. Phys. Chem. C* **2016**, *120*, 78−86.
(40) Zhao, X.; Gu, F.; Wang, Y.; Peng, Z.; Liu, J. Surface Electronegativity as an Activity Descriptor to Screen Oxygen Evolution Reaction Catalysts of Li−O_2 Battery. *ACS Appl. Mater. Interfaces* **2020**, *12*, 27166−27175.
(41) Poulain, R.; Klein, A.; Proost, J. Electrocatalytic Properties of (100)-, (110)-, and (111)-Oriented NiO Thin Films Toward the Oxygen Evolution Reaction. *J. Phys. Chem. C* **2018**, *122*, 22252−22263.
(42) Poulain, R.; Lumbeeck, G.; Hunka, J.; Proost, J.; Savolainen, H.; Idrissi, H.; Schryvers, D.; Gauquelin, N.; Klein, A. Electronic and Chemical Properties of Nickel Oxide Thin Films and the Intrinsic Defects Compensation Mechanism. *ACS Appl. Electron. Mater.* **2022**, *4*, 2718−2728.
(43) Radinger, H.; Connor, P.; Tengeler, S.; Stark, R. W.; Jaegermann, W.; Kaiser, B. Importance of Nickel Oxide Lattice Defects for Efficient Oxygen Evolution Reaction. *Chem. Mater.* **2021**, *33*, 8259−8266.
(44) Fu, G.; Wen, X.; Xi, S.; Chen, Z.; Li, W.; Zhang, J.-Y.; Tadich, A.; Wu, R.; Qi, D.-C.; Du, Y.; Cheng, J.; Zhang, K. H. L. Tuning the Electronic Structure of NiO via Li Doping for the Fast Oxygen Evolution Reaction. *Chem. Mater.* **2019**, *31*, 419−428.
(45) O'Neill, B. J.; Jackson, D. H. K.; Lee, J.; Canlas, C.; Stair, P. C.; Marshall, C. L.; Elam, J. W.; Kuech, T. F.; Dumesic, J. A.; Huber, G. W. Catalyst Design with Atomic Layer Deposition. *ACS Catal.* **2015**, *5*, 1804−1825.
(46) Anantharaj, S.; Kundu, S.; Noda, S. The Fe Effect": A Review Unveiling the Critical Roles of Fe in Enhancing OER Activity of Ni and Co Based Catalysts. *Nano Energy* **2021**, *80*, 105514.
(47) Klaus, S.; Louie, M. W.; Trotochaud, L.; Bell, A. T. Role of Catalyst Preparation on the Electrocatalytic Activity of Ni1−xFexOOH for the Oxygen Evolution Reaction. *J. Phys. Chem. C* **2015**, *119*, 18303−18316.
(48) Koushik, D.; Jošt, M.; Dučinskas, A.; Burgess, C.; Zardetto, V.; Weijtens, C.; Verheijen, M. A.; Kessels, W. M. M.; Albrecht, S.; Creatore, M. Plasma-Assisted Atomic Layer Deposition of Nickel

https://doi.org/10.1021/jacs.4c14493
J. Am. Chem. Soc. XXXX, XXX, XXX−XXX

Oxide as Hole Transport Layer for Hybrid Perovskite Solar Cells. *J. Mater. Chem. C* **2019**, *7*, 12532−12543.
(49) Lu, H. L.; Scarel, G.; Alia, M.; Fanciulli, M.; Ding, S.-J.; Zhang, D. W. Spectroscopic Ellipsometry Study of Thin NiO Films Grown on Si (100) by Atomic Layer Deposition. *Appl. Phys. Lett.* **2008**, *92* (22), 222907.
(50) Dovesi, R.; Erba, A.; Orlando, R.; Zicovich-Wilson, C. M.; Civalleri, B.; Maschio, L.; Rérat, M.; Casassa, S.; Baima, J.; Salustro, S.; et al. Quantum-Mechanical Condensed Matter Simulations with CRYSTAL. *Wiley Interdiscip. Rev.: Comput. Mol. Sci.* **2018**, *8* (4), No. e1360.
(51) Dovesi, R.; Pascale, F.; Civalleri, B.; Doll, K.; Harrison, N. M.; Bush, I.; D'Arco, P.; Noël, Y.; Rérat, M.; Carbonnière, P.; et al. The CRYSTAL code, 1976−2020 and beyond, a long story. *J. Chem. Phys.* **2020**, *152* (20), 204111.
(52) Adamo, C.; Barone, V. Toward Reliable Density Functional Methods Without Adjustable Parameters: The PBE0 model. *J. Chem. Phys.* **1999**, *110*, 6158−6170.
(53) Vilela Oliveira, D.; Laun, J.; Peintinger, M. F.; Bredow, T. BSSE-Correction Scheme for Consistent Gaussian Basis Sets of Double- and Triple-Zeta Valence with Polarization Quality for Solid-State Calculations. *J. Comput. Chem.* **2019**, *40*, 2364−2376.
(54) Grimme, S.; Antony, J.; Ehrlich, S.; Krieg, H. A Consistent and Accurate *Ab Initio* Parametrization of Density Functional Dispersion Correction (DFT-D) for the 94 Elements H-Pu. *J. Chem. Phys.* **2010**, *132* (15), 154104.
(55) Grimme, S.; Ehrlich, S.; Goerigk, L. Effect of the Damping Function in Dispersion Corrected Density Functional Theory. *J. Comput. Chem.* **2011**, *32*, 1456−1465.
(56) Ferrero, M.; Rérat, M.; Orlando, R.; Dovesi, R. The Calculation of Static Polarizabilities of 1−3D Periodic Compounds. The Implementation in the Crystal Code. *J. Comput. Chem.* **2008**, *29*, 1450−1459.
(57) Ferrero, M.; Rérat, M.; Kirtman, B.; Dovesi, R. Calculation of first and second static hyperpolarizabilities of one- to three-dimensional periodic compounds. Implementation in the CRYSTAL code. *J. Chem. Phys.* **2008**, *129* (24), 244110.
(58) Setyawan, W.; Curtarolo, S. High-Throughput Electronic Band Structure Calculations: Challenges and Tools. *Comput. Mater. Sci.* **2010**, *49*, 299−312.
(59) Momma, K.; Izumi, F. VESTA: A Three-Dimensional Visualization System for Electronic and Structural Analysis. *J. Appl. Crystallogr.* **2008**, *41*, 653−658.
(60) Jiang, W.; Lehnert, W.; Shviro, M. The Influence of Loadings and Substrates on the Performance of Nickel-Based Catalysts for the Oxygen Evolution Reaction. *ChemElectrochem* **2023**, *10* (2), No. e202200991.
(61) Horvai, G. Relationship Between Charge Transfer Resistance and Exchange Current Density of Ion Transfer at the Interface of Two Immiscible Electrolyte Solutions. *Electroanalysis* **1991**, *3*, 673−675.
(62) Wang, Z.; Goddard, W. A., III; Xiao, H. Potential-Dependent Transition of Reaction Mechanisms for Oxygen Evolution on Layered Double Hydroxides. *Nat. Commun.* **2023**, *14* (1), 4228.
(63) Shinagawa, T.; Garcia-Esparza, A. T.; Takanabe, K. Insight on Tafel Slopes from a Microkinetic Analysis of Aqueous Electrocatalysis for Energy Conversion. *Sci. Rep.* **2015**, *5* (1), 13801.
(64) Negahdar, L.; Zeng, F.; Palkovits, S.; Broicher, C.; Palkovits, R. Mechanistic Aspects of the Electrocatalytic Oxygen Evolution Reaction over Ni-Co Oxides. *ChemElectrochem* **2019**, *6*, 5588−5595.
(65) Antipin, D.; Risch, M. Calculation of the Tafel Slope and Reaction Order of the Oxygen Evolution Reaction Between pH 12 and pH 14 for the Adsorbate Mechanism. *Electrochem. Sci. Adv.* **2022**, *3* (6), No. e2100213.
(66) Nishimoto, T.; Shinagawa, T.; Naito, T.; Takanabe, K. Delivering the Full Potential of Oxygen Evolving Electrocatalyst by Conditioning Electrolytes at Near-Neutral pH. *ChemSuschem* **2021**, *14*, 1554−1564.
(67) Bredar, A. R. C.; Chown, A. L.; Burton, A. R.; Farnum, B. H. Electrochemical Impedance Spectroscopy of Metal Oxide Electrodes for Energy Applications. *ACS Appl. Energy Mater.* **2020**, *3*, 66−98.
(68) Nellist, M. R.; Laskowski, F. A. L.; Lin, F.; Mills, T. J.; Boettcher, S. W. Semiconductor-Electrocatalyst Interfaces: Theory, Experiment, and Applications in Photoelectrochemical Water Splitting. *Acc. Chem. Res.* **2016**, *49*, 733−740.
(69) Watzele, S.; Hauenstein, P.; Liang, Y.; Xue, S.; Fichtner, J.; Garlyyev, B.; Scieszka, D.; Claudel, F.; Maillard, F.; Bandarenka, A. S. Determination of Electroactive Surface Area of Ni-, Co-, Fe-, and Ir-Based Oxide Electrocatalysts. *ACS Catal.* **2019**, *9*, 9222−9230.
(70) Jeon, S. S.; Kang, P. W.; Klingenhof, M.; Lee, H.; Dionigi, F.; Strasser, P. Active Surface Area and Intrinsic Catalytic Oxygen Evolution Reactivity of NiFe LDH at Reactive Electrode Potentials Using Capacitances. *ACS Catal.* **2023**, *13*, 1186−1196.
(71) George, K.; Khachatrjan, T.; van Berkel, M.; Sinha, V.; Bieberle-Hütter, A. Understanding the Impact of Different Types of Surface States on Photoelectrochemical Water Oxidation: A Microkinetic Modeling Approach. *ACS Catal.* **2020**, *10*, 14649−14660.
(72) Zagalskaya, A.; Alexandrov, V. Role of Defects in the Interplay between Adsorbate Evolving and Lattice Oxygen Mechanisms of the Oxygen Evolution Reaction in RuO2 and IrO2. *ACS Catal.* **2020**, *10*, 3650−3657.
(73) Boukamp, B. Interpretation of the Gerischer Impedance in Solid State Ionics. *Solid State Ionics* **2003**, *157*, 29−33.
(74) Adler, S. B.; Lane, J. A.; Steele, B. C. H. Electrode Kinetics of Porous Mixed-Conducting Oxygen Electrodes. *J. Electrochem. Soc.* **1996**, *143*, 3554−3564.
(75) Yasin, L.; Atkinson, A.; Cooper, S. J.; Bertei, A. Identifiability of the Mechanisms Governing the Reaction Kinetics of MIEC Electrodes in Solid Oxide Cells. *Electrochim. Acta* **2023**, *472*, 143418.
(76) Wang, Z.; Guo, X.; Montoya, J.; Nørskov, J. K. Predicting Aqueous Stability of Solid with Computed Pourbaix Diagram Using SCAN Functional. *Npj Comput. Mater.* **2020**, *6* (1), 160.
(77) Winter, M.; Brodd, R. J. What Are Batteries, Fuel Cells, and Supercapacitors? *Chem. Rev.* **2004**, *104*, 4245−4270.
(78) Schindler, S.; Bauer, M.; Petzl, M.; Danzer, M. A. Voltage Relaxation and Impedance Spectroscopy as In-Operando Methods for the Detection of Lithium Plating on Graphitic Anodes in Commercial Lithium-Ion Cells. *J. Power Sources* **2016**, *304*, 170−180.
(79) Mackus, A. J. M.; Schneider, J. R.; MacIsaac, C.; Baker, J. G.; Bent, S. F. Synthesis of Doped, Ternary, and Quaternary Materials by Atomic Layer Deposition: A Review. *Chem. Mater.* **2019**, *31*, 1142−1183.
(80) Napari, M.; Huq, T. N.; Hoye, R. L. Z.; MacManus-Driscoll, J. L. Nickel Oxide Thin Films Grown by Chemical Deposition Techniques: Potential and Challenges in Next-Generation Rigid and Flexible Device Applications. *InfoMat* **2021**, *3*, 536−576.
(81) Hossain, M. A.; Zhang, T.; Zakaria, Y.; Lambert, D.; Burr, P.; Rashkeev, S.; Abdallah, A.; Hoex, B. Doped Nickel Oxide Carrier-Selective Contact for Silicon Solar Cells. *IEEE J. Photovoltaics* **2021**, *11*, 1176−1187.
(82) Weng, L.-T. Advances in the Surface Characterization of Heterogeneous Catalysts Using ToF-SIMS. *Appl. Catal., A* **2014**, *474*, 203−210.
(83) Biesinger, M. C.; Payne, B. P.; Lau, L. W. M.; Gerson, A.; Smart, R. S. C. X-ray Photoelectron Spectroscopic Chemical State Quantification of Mixed Nickel Metal, Oxide and Hydroxide Systems. *Surf. Interface Anal.* **2009**, *41*, 324−332.
(84) Grosvenor, A. P.; Biesinger, M. C.; Smart, R. S.; McIntyre, N. S. New Interpretations of XPS Spectra of Nickel Metal and Oxides. *Surf. Sci.* **2006**, *600*, 1771−1779.
(85) Marrani, A. G.; Novelli, V.; Sheehan, S.; Dowling, D. P.; Dini, D. Probing the Redox States at the Surface of Electroactive Nanoporous NiO Thin Films. *ACS Appl. Mater. Interfaces* **2014**, *6*, 143−152.
(86) Mansour, A. N. Characterization of $LiNiO_2$ by XPS. *Surf. Sci. Spectra.* **1994**, *3*, 279−286.

https://doi.org/10.1021/jacs.4c14493
J. Am. Chem. Soc. XXXX, XXX, XXX−XXX

(87) Mansour, A. N.; Melendres, C. A. Characterization of α-$Ni(OH)_2$ by XPS. *Surf. Sci. Spectra.* **1994**, *3*, 255−262.
(88) Payne, B.; Biesinger, M.; McIntyre, N. The Study of Polycrystalline Nickel Metal Oxidation by Water Vapour. *J. Electron Spectrosc. Relat. Phenom.* **2009**, *175*, 55−65.
(89) Toparli, C.; Sarfraz, A.; Wieck, A. D.; Rohwerder, M.; Erbe, A. In Situ and Operando Observation of Surface Oxides During Oxygen Evolution Reaction on Copper. *Electrochim. Acta* **2017**, *236*, 104−115.
(90) Kavan, L. Electrochemistry and band structure of semiconductors (TiO_2, SnO_2, ZnO): Avoiding Pitfalls and Textbook Errors. *J. Solid State Electrochem.* **2024**, *28*, 829−845.
(91) Thürmer, S.; Malerz, S.; Trinter, F.; Hergenhahn, U.; Lee, C.; Neumark, D. M.; Meijer, G.; Winter, B.; Wilkinson, I. Accurate Vertical Ionization Energy and Work Function Determinations of Liquid Water and Aqueous Solutions. *Chem. Sci.* **2021**, *12*, 10558−10582.
(92) Tao, H. B.; Fang, L.; Chen, J.; Yang, H. B.; Gao, J.; Miao, J.; Chen, S.; Liu, B. Identification of Surface Reactivity Descriptor for Transition Metal Oxides in Oxygen Evolution Reaction. *J. Am. Chem. Soc.* **2016**, *138*, 9978−9985.
(93) Anantharaj, S.; Sugime, H.; Noda, S. Why Shouldn't Double-Layer Capacitance (be Always Trusted to Justify Faradaic Electrocatalytic Activity Differences? *J. Electroanal. Chem.* **2021**, *903*, 115842.
(94) Rao, R. R.; Corby, S.; Bucci, A.; García-Tecedor, M.; Mesa, C. A.; Rossmeisl, J.; Giménez, S.; Lloret-Fillol, J.; Stephens, I. E. L.; Durrant, J. R. Spectroelectrochemical Analysis of the Water Oxidation Mechanism on Doped Nickel Oxides. *J. Am. Chem. Soc.* **2022**, *144*, 7622−7633.
(95) Iandolo, B.; Hellman, A. The Role of Surface States in the Oxygen Evolution Reaction on Hematite. *Angew. Chem., Int. Ed.* **2014**, *53*, 13404−13408.
(96) Bhattacharjee, S.; Waghmare, U. V.; Lee, S.-C. An improved d-band model of the catalytic activity of magnetic transition metal surfaces. *Sci. Rep.* **2016**, *6* (1), 35916.
(97) Ruban, A.; Hammer, B.; Stoltze, P.; Skriver, H.; Nørskov, J. Surface Electronic Structure and Reactivity of Transition and Noble Metals. Communication Presented at the First Francqui Colloquium, Brussels, 19−20 February 1996.1. *J. Mol. Catal. A: Chem.* **1997**, *115*, 421−429.
(98) Zhang, J.; Yang, H. B.; Zhou, D.; Liu, B. Adsorption Energy in Oxygen Electrocatalysis. *Chem. Rev.* **2022**, *122*, 17028−17072.
(99) Moltved, K. A.; Kepp, K. P. The Chemical Bond between Transition Metals and Oxygen: Electronegativity, d-Orbital Effects, and Oxophilicity as Descriptors of Metal−Oxygen Interactions. *J. Phys. Chem. C* **2019**, *123*, 18432−18444.
(100) Linnera, J.; Sansone, G.; Maschio, L.; Karttunen, A. J. Thermoelectric Properties of p-Type Cu2O, CuO, and NiO from Hybrid Density Functional Theory. *J. Phys. Chem. C* **2018**, *122*, 15180−15189.
(101) Bueno, P. R.; Davis, J. J. Measuring Quantum Capacitance in Energetically Addressable Molecular Layers. *Anal. Chem.* **2014**, *86*, 1337−1341.
(102) Bueno, P. R.; Feliciano, G. T.; Davis, J. J. Capacitance Spectroscopy and Density Functional Theory. *Phys. Chem. Chem. Phys.* **2015**, *17*, 9375−9382.
(103) Bueno, P. R.; Bedatty Fernandes, F. C.; Davis, J. J. Quantum Capacitance as a Reagentless Molecular Sensing Element. *Nanoscale* **2017**, *9*, 15362−15370.
(104) Božič, A.; Podgornik, R. Site Correlations, Capacitance, and Polarizability From Protein Protonation Fluctuations. *J. Phys. Chem. B* **2021**, *125*, 12902−12908.
(105) Loco, D.; Lagardère, L.; Adjoua, O.; Piquemal, J.-P. Atomistic Polarizable Embeddings: Energy, Dynamics, Spectroscopy, and Reactivity. *Acc. Chem. Res.* **2021**, *54*, 2812−2822.
(106) Østrøm, I.; Ortolan, A. O.; Caramori, G. F.; Mascal, M.; Muñoz-Castro, A.; Parreira, R. L. T. In Silico Design of Cylindrophanes: The Role of Functional Groups in a Fluoride Selective Host. *ChemPhyschem* **2020**, *21*, 1989−2005.
(107) Miller, T. M.; Bederson, B. *Advances in Atomic and Molecular Physics Vol. 25*; Elsevier, 1989; pp. 37−60.
(108) Halldin Stenlid, J.; Johansson, A. J.; Brinck, T. The Local Electron Attachment Energy and the Electrostatic Potential as Descriptors of Surface−Adsorbate Interactions. *Phys. Chem. Chem. Phys.* **2019**, *21*, 17001−17009.
(109) Raupach, M.; Tonner, R. A Periodic Energy Decomposition Analysis Method for the Investigation of Chemical Bonding in Extended Systems. *J. Chem. Phys.* **2015**, *142* (19), 194105.

https://doi.org/10.1021/jacs.4c14493
J. Am. Chem. Soc. XXXX, XXX, XXX−XXX